

Unified Manipulability and Compliance Analysis of Modular Soft-Rigid Hybrid Fingers

Jianshu Zhou, Boyuan Liang, Junda Huang, and
Masayoshi Tomizuka

*Department of Mechanical Engineering, University of California,
Berkeley (e-mail: [jianshuzhou@berkeley.edu, liangb@berkeley.edu,
ustcdraja@gmail.com, tomizuka@berkeley.edu]).*

Abstract: This paper presents a unified framework to analyze the manipulability and compliance of modular soft-rigid hybrid robotic fingers. The approach applies to both hydraulic and pneumatic actuation systems. A Jacobian-based formulation maps actuator inputs to joint and task-space responses. Hydraulic actuators are modeled under incompressible assumptions, while pneumatic actuators are described using nonlinear pressure–volume relations. The framework enables consistent evaluation of manipulability ellipsoids and compliance matrices across actuation modes. We validate the analysis using two representative hands: DexCo (hydraulic) and Edgy-2 (pneumatic). Results highlight actuation-dependent trade-offs in dexterity and passive stiffness. These findings provide insights for structure-aware design and actuator selection in soft-rigid robotic fingers.

Keywords: Soft-rigid Hybrid Actuation, Manipulability Analysis, Compliance Modeling, Modular Robotic Fingers

1. INTRODUCTION

Achieving dexterous and robust manipulation in unstructured environments remains a core challenge in robotics (Billard and Kragic, 2019). As robotic hands advance beyond simple grasping toward versatile in-hand manipulation, there is growing demand for systems that combine precise control, adaptability, compliance, and safe physical interaction. *Soft robotic systems* excel in adaptive grasping through material compliance and morphology-driven control but face limitations in precision tasks. *Soft-rigid hybrid systems*, which integrate compliant actuators with rigid linkages, offer a balanced approach—enabling both fine control and structural adaptability.

A variety of soft and soft-rigid robotic hands has emerged over the past decade. Pneumatic systems like the RBO Hand (Deimel and Brock, 2016) and the Pisa/IIT Soft-Hand (Catalano et al., 2014) enable compliant grasping via soft inflation or tendon-driven underactuation. Hybrid hands enhance control and robustness by combining soft actuators with rigid structures, including origami mechanisms (Li et al., 2019), layer jamming (Manti et al., 2016), bellow-type encapsulation (Lee et al., 2024), and geometric confinement (Zhang et al., 2020). Variable stiffness (Wolf et al., 2015) and programmable actuation (Polygerinos et al., 2017) further boost adaptability.

Our prior work explores both soft and soft-rigid hands. The gripper in (Zhou et al., 2017) uses textured dual-chamber fingers for low-pressure adaptation. The BCL-26 hand (Zhou et al., 2019) achieves human-like motion with 26 fiber-reinforced soft degrees of freedom (DOFs).

We incorporated stiffness tuning via particle jamming in (Zhou et al., 2020). The DexCo Hand (Zhou et al., 2024) uses hydraulic actuation for forceful, controllable motion, while the Edgy-2 Hand (Zhou et al., 2018) emphasizes modular pneumatic flexibility.

Despite recent advances, many studies remain focused on empirical evaluation and lack generalizable models for analyzing or comparing design variants. While task-specific tuning may suffice for grasping, manipulation tasks demand predictive insights into how structure and actuation affect performance. Two key metrics—*manipulability*, describing motion capability (Doty et al., 1995), and *compliance*, capturing passive deformation under force (Aukes et al., 2014)—are essential for assessing dexterity and adaptability. Though common in rigid and underactuated systems, these metrics are rarely jointly analyzed in soft-rigid hybrid designs, especially across different actuation modes. This gap hinders structure-aware design and cross-system performance generalization.

To address this, we propose a unified analytical framework for evaluating both manipulability and compliance in modular soft-rigid hybrid fingers actuated by hydraulic or pneumatic systems. We formulate a Jacobian-based model that maps actuator inputs to joint and task-space behaviors. Hydraulic systems are modeled using a linear approximation under incompressible flow, while pneumatic actuators are captured using nonlinear pressure–volume relationships derived from ideal gas behavior (Polygerinos et al., 2017). This formulation enables consistent computation of manipulability ellipsoids and compliance matrices across actuation types. We validate the proposed frame-

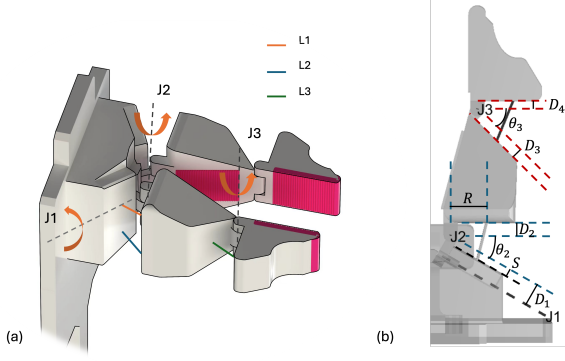


Fig. 1. (a) Kinematic model of linear soft actuators: dashed lines (J1–J3) denote passive revolute joints; solid lines (L1–L3) represent soft actuators. (b) Top view of a DexCo finger at $\theta_1 = 0$, with parameters used in (1) and (2) labeled.

work on two representative systems: the hydraulically actuated *DexCo Hand* and the pneumatically actuated *Edgy-2 Hand*. Simulation and experimental results reveal actuation-dependent trade-offs in directional dexterity and passive stiffness, offering insights for structure-aware analysis, actuator selection, and modular finger design in soft-rigid robotic fingers.

2. MANIPULABILITY ANALYSIS

To analyze the manipulability of the soft-rigid hybrid fingers, we begin with an approximate model that represents the soft actuators as soft linear actuators. Considering the inherent flexibility of soft actuators, we further assume that the soft linear actuators are connected to the knuckles of the DexCo hand via universal joints at both ends. Given the attachment points of the actuators in the local frame of each knuckle, and the poses of the revolute joints, the length of each linear soft actuator corresponds to the distance between its respective attachment points. A visualization of this model is provided in Fig. 1a.

This section analyzes the kinematic mapping between the lengths of the linear soft actuators, denoted as l_1 , l_2 and l_3 and the poses of the passive revolute joints, denoted as θ_1 , θ_2 , θ_3 . Based on visual inspection of Fig. 1, this mapping can be decomposed into two parts: θ_3 depends solely on l_3 while θ_1 and θ_2 are jointly determined by l_1 and l_2 . The remainder of this section discusses each of these relationships in detail and validates them via hardware experiments.

2.1 Dual Soft Actuation Case

This subsection investigates the kinematic relationship between l_1 , l_2 and the joint angles θ_1 , θ_2 . Through geometric analysis, this relationship can be expressed as follows:

$$\begin{aligned} l_1^2 &= A^2 + (H \cos \theta_1 - V \sin \theta_1 - S)^2 \\ &\quad + (H \sin \theta_1 + V \cos \theta_1 - V)^2 \\ l_2^2 &= A^2 + (H \cos \theta_1 + V \sin \theta_1 - S)^2 \\ &\quad + (H \sin \theta_1 - V \cos \theta_1 + V)^2 \end{aligned} \quad (1)$$

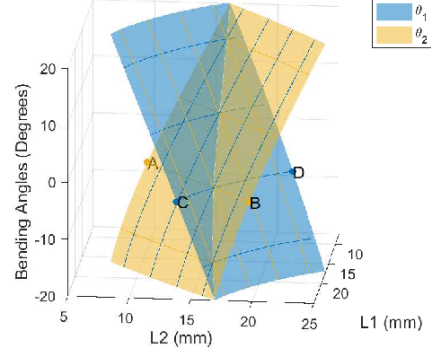


Fig. 2. Surface plot that maps l_1 and l_2 into θ_1 and θ_2 . Yellow lines represent sets of l_1 and l_2 combinations where θ_1 remains the same, while blues lines are sets where θ_2 remains the same.

Here, A , H , and V represent the axial, horizontal, and vertical offsets, respectively, from joint J_1 to joint J_2 , as functions of θ_2 when $\theta_1 = 0$. These offsets can be computed as follows. The parameter R denotes the radial distance from the attachment points of actuators L_1 and L_2 to the axis of joint J_2 . The quantities D_1 and D_2 represent the offsets between the actuator attachment surface and the rotation axes. The parameter S denotes the horizontal distance from joint J_1 to the actuator base attachment point, as shown in Fig. 1b. Lastly, L is the distance between the actuator endpoints on the attachment surface.

$$\begin{aligned} A &= R(1 - \cos \theta_2) + D_2 \sin \theta_1 \\ H &= D_1 + R \sin \theta_2 + D_2 \cos \theta_2 \\ V &= \frac{L}{2} \end{aligned} \quad (2)$$

Fig. 2 illustrates the mapping between (l_1, l_2) and (θ_1, θ_2) . We fix θ_1 at -15° , -5° , 5° , and 15° , and plot the corresponding contour lines on the resulting surface. By vertically projecting these contour lines onto the θ_2 surface, we obtain curves that represent the achievable range of θ_2 through appropriate adjustment of l_1 and l_2 . Similarly, another set of curves is generated to represent the achievable range of θ_1 while holding θ_2 fixed. The analysis is constrained to the range $[-20^\circ, 20^\circ]$ for both θ_1 and θ_2 , as configurations beyond this range may result in self-collisions. The plots show that for each fixed value of θ_1 or θ_2 , the other joint can still achieve the full range of $[-20^\circ, 20^\circ]$ through suitable adjustment of l_1 and l_2 . This suggests that the pose of joint J_1 or J_2 has limited influence on the reachable workspace of the other joint.

To further analyze the relationship between actuator inputs and joint configurations, we plot the projected curves along the contour directions, as shown in Fig. 3a. The two contour paths are defined from point A to B and from point C to D, as indicated in Fig. 2. The x-axis values in these plots correspond to a normalized actuator motion (denoted as NAM). Taking the contour from A to B as an example, for a given point (l_1, l_2, θ_1) on the contour, and letting $(l_{1,A}, l_{2,A}, \theta_1)$ denote the coordinates at point A, the normalized actuator motion is computed as follows:

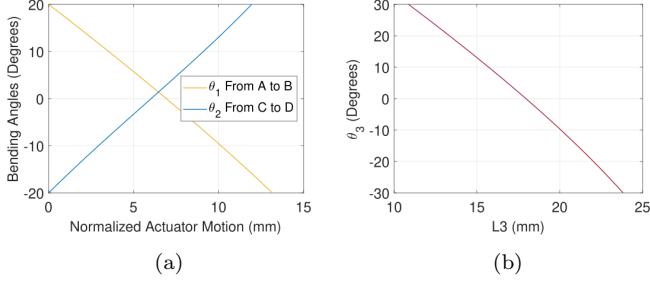


Fig. 3. (a): The projected curves for contours from A to B and from C to D. The positions of A, B, C, D are marked in Fig. 2. (b): J3 pose against soft actuator L3 length.

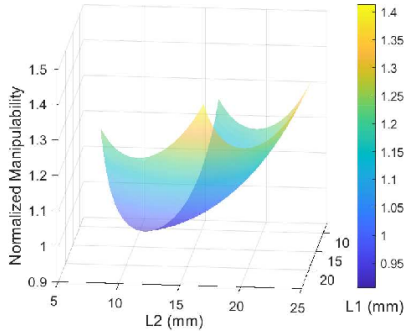


Fig. 4. Normalized manipulability distribution.

$$NAM = \sqrt{(l_1 - l_{1,A})^2 + (l_2 - l_{2,A})^2} \quad (3)$$

As shown in the left side of Fig. 3, the motion of joints J_1 and J_2 exhibits an approximately linear relationship with respect to the normalized actuator motion, with a slope of approximately $3.5^\circ/\text{mm}$. This slope represents a balanced value, neither too steep nor too shallow, indicating that the soft actuators can effectively drive the passive joints without requiring excessive effort. At the same time, the passive joints are not overly sensitive to small variations in actuator motion, contributing to stable and controllable behavior.

Fig. 4 presents the manipulability, M , analysis over the entire workspace. The manipulability is computed using the following equation, which characterizes the actuator effort required to produce joint motions in arbitrary directions.

$$M = \left| \det \begin{bmatrix} \frac{\partial \theta_1}{\partial l_1} & \frac{\partial \theta_1}{\partial l_2} \\ \frac{\partial \theta_2}{\partial l_1} & \frac{\partial \theta_2}{\partial l_2} \end{bmatrix} \right| = \left(\left| \det \begin{bmatrix} \frac{\partial l_1}{\partial \theta_1} & \frac{\partial l_1}{\partial \theta_2} \\ \frac{\partial l_2}{\partial \theta_1} & \frac{\partial l_2}{\partial \theta_2} \end{bmatrix} \right| \right)^{-1} \quad (4)$$

The partial derivatives are directly obtained from (1). To eliminate the influence of unit selection, the manipulability can be normalized by dividing it by its value at the reference configuration where $\theta_1 = \theta_2 = 0$. As shown in Fig. 4, the normalized manipulability remains well-conditioned across the workspace, without exhibiting any extreme or anomalous values.

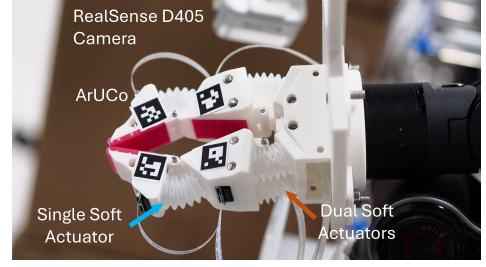


Fig. 5. Experimental setup. The joint angles are captured from ArUco code ((Romero-Ramirez et al., 2018)).

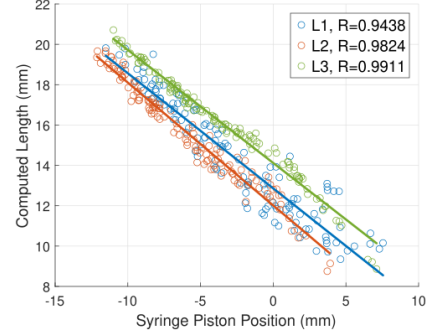


Fig. 6. Linear regressions for hydraulic actuator lengths l^e against syringe piston positions Q^e in the experiments.

2.2 Single Soft Actuation Case

This section investigates the relationship between l_3 and θ_3 . Through direct analytical computation, the following expression can be derived:

$$\begin{aligned} l_3^2 &= H_3^2 + V_3^2 \\ H_3 &= D_3 + R \sin \theta_3 + D_4 \cos \theta_3 \\ V_3 &= R(1 - \cos \theta_3) + D_4 \sin \theta_3 \end{aligned} \quad (5)$$

The parameters D_3 and D_4 represent the offsets between the soft actuator attachment surface and the rotational axes, as illustrated in Fig. 1b. From this configuration, it can be observed in Fig. 3b that θ_3 exhibits an approximately linear relationship with l_3 , with a slope of about $5^\circ/\text{mm}$. This suggests that joint J_3 responds to actuator L_3 with a balanced sensitivity, neither overly responsive nor excessively resistant to input, indicating effective and stable actuation.

2.3 Experimental Validation with Hydraulic Actuators

To validate the models proposed in (1) and (5), we conducted experiments using a physical DexCo hand equipped with hydraulic actuators L_1 , L_2 , and L_3 . These actuators are filled with incompressible liquid and actuated by three independent external syringes. Let Q_1 , Q_2 , and Q_3 denote the piston positions of the corresponding syringes. An increase in Q indicates that liquid is being withdrawn from the actuator, resulting in a decrease in actuator length.

Due to the near-incompressibility of the liquid under room temperature and moderate pressure, the actuator lengths l are expected to maintain an affine relationship with the

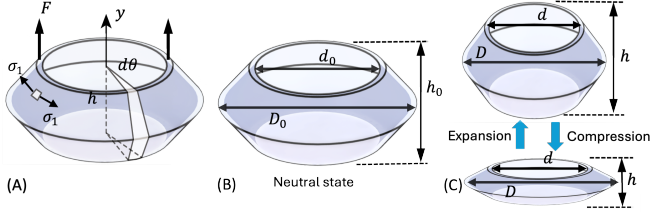


Fig. 7. (A) Compliance modeling for force estimation in actuation space. (B) Initial state of the origami bellow. (C) Extended and contracted states.

piston positions, i.e., $l = kQ + b$, where k and b are scalar coefficients determined experimentally. Based on this assumption, we collected 200 data samples of the form $(Q_1^e, Q_2^e, Q_3^e, \theta_1^e, \theta_2^e, \theta_3^e)$, and computed the corresponding expected actuator lengths l_1^e , l_2^e , and l_3^e . Linear regression was then performed between the pairs (Q_1^e, l_1^e) , (Q_2^e, l_2^e) , and (Q_3^e, l_3^e) , as illustrated in Fig. 6. The results demonstrate a strong linear correlation between actuator lengths and piston positions, with high coefficients of determination, validating the geometric models in (1) and (5). The slightly higher variance observed in the L1 data may be attributed to minor misalignment or increased friction in its tubing connection, which affects the repeatability of piston-to-length translation in the physical setup.

2.4 Potential Extension to Pneumatic Actuators

It is worth noting that the geometric modeling presented in Sections 2.1 and 2.2 constitutes a generalizable framework that can also be applied to pneumatic actuators. While air is typically treated as a compressible fluid, it is common practice to establish a mapping from the piston position Q and the pressure within the syringe P to the actuator length l through experimental calibration. Once this mapping is identified, it becomes possible to derive the relationship between (Q, P) and the resulting joint configurations.

3. COMPLIANCE MODELING

While manipulability characterizes motion capability, compliance captures the response to external forces—an equally critical aspect in soft-rigid design. Owing to material softness, both hydraulic and pneumatic actuators exhibit inherent compliance during interaction. This section presents a static analysis and compliance modeling of the soft-rigid hybrid hand, mapping actuation inputs (\mathbf{a}) to joint configurations ($\boldsymbol{\tau}$). We develop models for the compliance introduced by hydraulic and pneumatic actuation and validate them through object manipulation simulations.

3.1 Hydraulic Compliance Modeling

In hydraulic systems, compliance arises primarily from the compressibility of the working fluid, the elasticity of the fluidic chamber and tubing, and the mechanical compliance of the structure.

Compared to traditional hydraulic systems that exhibit high stiffness and low compliance, the dominant source

of compliance in soft hydraulic actuators is the elastic deformation of the chamber material, characterized by its Young's modulus E . As the material deforms under pressure, the internal diameter changes from its undeformed size D_0 and d_0 to the deformed value D and d thereby altering the internal geometry and enabling displacement. The hydraulic force in soft actuators arises from the elastic deformation of the material in the axial direction during compression or extension, similar to inflating a balloon (Fig. 7).

We assume under an initial height h_0 of the soft actuator, the volume of water remains constant during motion, i.e., $V = V_0 \triangleq \text{constant}$. Based on this assumption, the geometric constraint is given by:

$$\begin{aligned} V_0 &= \frac{\pi h_0}{3} \left[\left(\frac{D_0}{2} \right)^2 + \left(\frac{d_0}{2} \right)^2 + \frac{D_0 d_0}{4} \right] \\ V &= \frac{\pi h}{3} \left[\left(\frac{D}{2} \right)^2 + \left(\frac{d}{2} \right)^2 + \frac{Dd}{4} \right] \\ V &= V_0 \end{aligned} \quad (6)$$

To evaluate the radial deformation, we apply thin-walled pressure vessel theory. As illustrated in Fig. 7, the hoop stress σ_1 is calculated along the actuator's axial profile:

$$\sigma_1 = \frac{Pr}{t} \quad (7)$$

where r is the local radius at height y , P is the internal pressure, and t is the wall thickness. According to the generalized Hooke's law, the circumferential strain ε_1 is:

$$\varepsilon_1 = \frac{\sigma_1}{E} = \frac{\Delta_\ell}{2\pi r} \quad (8)$$

where Δ_ℓ denotes the change in circumference due to radial expansion, i.e., $\Delta_\ell = 2\pi(r - r_0)$, with r_0 representing the undeformed radius and r the deformed radius. Using (7) and (8), we derive the expressions for the deformed inner and outer diameters under pressure P via replacing r with $\frac{d_0}{2}$ and $\frac{D_0}{2}$:

$$\begin{aligned} d &= d_0 + \frac{2P}{Et} \left(\frac{d_0}{2} \right)^2 \\ D &= D_0 + \frac{2P}{Et} \left(\frac{D_0}{2} \right)^2 \end{aligned} \quad (9)$$

where the internal pressure is defined as $P \triangleq -\frac{4}{\pi d_0^2} F_h$. Substituting (9) into (6), we can solve for the hydraulic force $F_h = F_h(h_0, \Delta y)$ by solving a resulting quadratic equation.

To characterize the pressure-to-displacement relationship of the hydraulic actuator, we define two compliance-related parameters. The first is the hydraulic compliance C_h , which reflects the actuator's deformation response to external force and is expressed as displacement per unit force. To translate this into a form compatible with pressure input modeling, we introduce the effective linear compliance $C_l = C_h/A$, where A denotes the actuator's effective cross-sectional area. This conversion yields a

linear input-output relationship between internal pressure P and output displacement l , given by $l = C_l \cdot P$. This formulation allows for consistent integration of actuator compliance into the Jacobian-based framework for joint-space stiffness and task-space compliance analysis.

In joint space, the Jacobian matrix $J \in \mathbb{R}^{n \times m}$ relates joint displacements $\Delta q \in \mathbb{R}^m$ to end-effector displacements $\Delta l \in \mathbb{R}^n$ via $\Delta l = J \cdot \Delta q$, as defined in Equation (4). Under an external force $\Delta f \in \mathbb{R}^n$, the resulting torque deviation in joint space $\Delta \tau \in \mathbb{R}^m$ can be expressed as:

$$\Delta \tau = J^T \cdot \Delta f = J^T \cdot \frac{1}{C_l} \cdot \Delta l = \frac{1}{C_l} J^T J \cdot \Delta q \quad (10)$$

Here, C_l is the effective linear compliance that maps input pressure to displacement. Based on this relationship, we derive the joint-space stiffness matrix $K_q \in \mathbb{R}^{m \times m}$ and its inverse (i.e., joint-space compliance matrix C_q) as:

$$K_q = \frac{1}{C_l} J^T J, \quad C_q = K_q^{-1} = C_l \cdot (J^T J)^{-1} \quad (11)$$

To analyze system behavior in task space, we transform these joint-space matrices using a task-space Jacobian $J_a \in \mathbb{R}^{n \times m}$, leading to:

$$\begin{aligned} K_a &= J_a^T K_q J_a \\ J_a C_a J_a^T &= C_q \end{aligned} \quad (12)$$

where K_a and C_a are the task-space stiffness and compliance matrices, respectively. This transformation reveals how global actuator compliance C_l interacts with configuration-dependent geometry (via J and J_a) to shape the directional compliance profile in task space.

This result is analogous to classical manipulability-based compliance analysis, revealing how the hydraulic compliance C_l globally scales the configuration-dependent compliance profile.

3.2 Pneumatic Actuation Model

In pneumatic systems, the input pressure is indirectly regulated via flow control, and the resulting output force is strongly dependent on chamber volume, which changes with deformation. Therefore the geometric constrain assumption made in hydraulic actuation is not ever applicable (6).

Assuming quasi-static behavior and ideal gas behavior, we model the internal pressure as:

$$P(l) = \frac{nRT}{V(l)} = \frac{nRT}{V_0 + \alpha l} \quad (13)$$

where l is the deformation-dependent variable (e.g., finger length or curvature), and α is a volume gain coefficient. The corresponding output force is:

$$f(l) = \beta P(l) = \beta \cdot \frac{nRT}{V_0 + \alpha l} \quad (14)$$

This nonlinear relation suggests a decreasing output force with increasing deformation, introducing variable stiffness properties in the actuation. When mapped to joint space via the Jacobian, the torque is:

$$\tau = J^T(q) f(q) \quad (15)$$

highlighting the pressure-volume-deformation coupling in the control of soft-rigid pneumatic systems.

Experimental validation of pressure-deformation behavior in our previous work (Zhou et al., 2018) supports the pneumatic modeling in this work.

3.3 Simulate Compliance Motion

In simulation, we focus on simulating the hydraulic compliance. The variable stiffness property inherent in the DexCo hand can be modeled either as a linear variable elastic force, expressed as follows:

$$\tau_k = -k(\theta_0) \Delta \theta \quad (16)$$

where θ_0 is the joint angle in the absence of external forces, θ is the current joint angle, and $\Delta \theta = \theta - \theta_0$ denotes the angular deformation. The linear elastic force in Eq. 16 can be transformed into Cartesian space using the stiffness matrix $K_a = J_a^T K_q J_a$, where J_a is the Jacobian and K_q is the joint stiffness matrix.

When modeling the stiffness as a torque input in simulation, it affects the system dynamics as follows:

$$M(\theta) \ddot{\theta} + H(\dot{\theta}, \theta) + G = \tau_k \quad (17)$$

In Eq. 17, the left-hand side captures inertial, Coriolis, and gravitational effects computed by the Gazebo simulator. The right-hand term, τ_k , represents torques from elastic deformation. Incorporating τ_k enables simulation of nonlinear variable stiffness behaviors, as shown in Fig. 8B.

The simulation involves two phases: a compliant caging grasp to enclose the object, followed by forceful release via increased base joint actuation and fingertip reorientation. Fig. 8A shows both commanded and actual joint angles. Compliance-induced deviations are observed between target and actual responses, where Joints 2 and 3 form the base, and Joint 4 corresponds to the fingertip.

4. CONCLUSION

This paper presents a unified framework for analyzing the manipulability and compliance of modular soft-rigid hybrid fingers actuated by hydraulic and pneumatic systems. Using a generalized Jacobian-based formulation, we enable consistent structural evaluation of directional dexterity and passive compliance across actuation modes. Experimental validation on the DexCo (hydraulic) and Edgy-2 (pneumatic) hands highlights key trade-offs between actuation type, structure, and control sensitivity.

Our results highlight that control response and actuation speed are distinct in hybrid systems. As shown in Table 1, hydraulic actuators enable precise control but slower

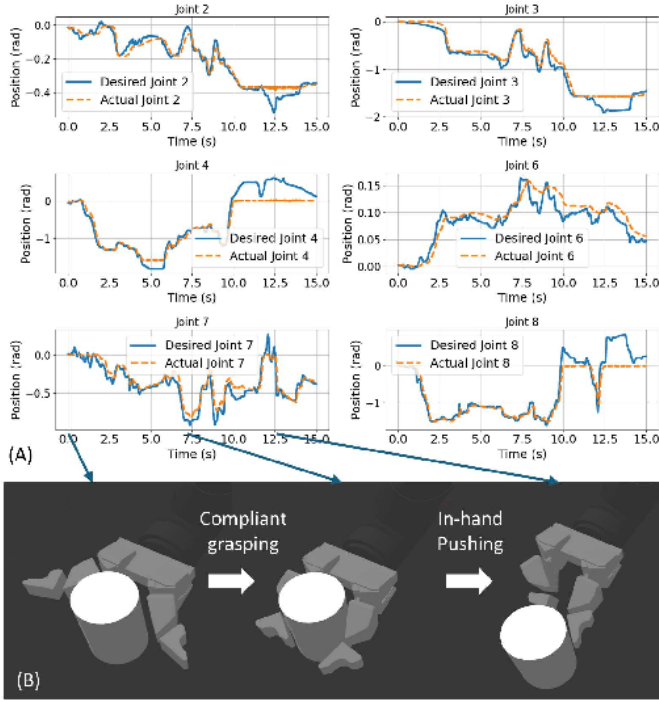


Fig. 8. Compliant motion simulation of the Soft-Rigid hybrid hand in Gazebo: (A) joint trajectories; (B) final interaction state.

motion, while pneumatic actuators offer faster deformation with less stability. These mismatches suggest the need for functional separation or hierarchical integration in control design.

Table 1. Summary of actuation trade-offs.

Metric	Hydraulic	Pneumatic
Control response speed	Fast	Slow
Actuation speed	Slower	Faster
Force output precision	High	Low-moderate
Passive compliance	Low	High

We recommend structure-aware and actuation-aware design principles, including: (1) avoiding direct coupling of mismatched subsystems; (2) assigning distinct roles to each actuator type (e.g., pneumatic for grasping, hydraulic for in-hand manipulation); and (3) leveraging our framework to assess design trade-offs early in development.

While the current formulation focuses on quasi-static behavior, future work will incorporate dynamic effects such as inertia and damping, particularly for soft-rigid hybrid fingers. We also aim to extend the framework to include contact interactions and grasp stability for task-level analysis and robust control.

REFERENCES

Aukes, D.M., Heyneman, B., Ulmen, J., Stuart, H., Cutkosky, M.R., Kim, S., and Edsinger, A. (2014). Design and testing of a selectively compliant underactuated hand. *The International Journal of Robotics Research*, 33(5), 721–735.

Billard, A. and Kragic, D. (2019). Trends and challenges in robot manipulation. *Science*, 364(6446), eaat8414.

Catalano, M.G., Grioli, G., Farnioli, E., Serio, A., Piazza, C., and Bicchi, A. (2014). Adaptive synergies for the

design and control of the pisa/iit soffhand. In *Proceedings of the 2014 IEEE/RAS International Conference on Humanoid Robots*, 497–503.

Deimel, R. and Brock, O. (2016). A novel type of compliant and underactuated robotic hand for dexterous grasping. *The International Journal of Robotics Research*, 35(1–3), 161–185.

Doty, K.L., Melchiorri, C., Schwartz, E.M., and Bonivento, C. (1995). Robot manipulability. *IEEE Transactions on Robotics and Automation*, 11(3), 462–468.

Lee, P.S., Sjaarda, C., Gao, R.Z., Dupuis, J., Rukavina-Nolsoe, M., and Ren, C.L. (2024). Soft-rigid hybrid revolute and prismatic joints using multilayered bellows-type soft pneumatic actuators: Design, characterization, and its application as soft-rigid hybrid gripper. *Soft Robotics*.

Li, S., Yuk, H., Guo, H.Y., Zhao, X., Cui, L., and Zhao, X. (2019). A stretchable and foldable origami robot for crawling and object transport. *Science Robotics*, 4(37), eaax1594.

Manti, M., Cacucciolo, V., and Cianchetti, M. (2016). Stiffening in soft robotics: A review of the state of the art. *IEEE Robotics & Automation Magazine*, 23(3), 93–106.

Polygerinos, P., Wang, Z., Galloway, K.C., Wood, R.J., and Walsh, C.J. (2017). Soft robotics: Review of fluid-driven intrinsically soft devices; manufacturing, sensing, control, and applications in human-robot interaction. *Advanced Engineering Materials*, 19(12), 1700016.

Romero-Ramirez, F.J., Muñoz-Salinas, R., and Medina-Carnicer, R. (2018). Speeded up detection of squared fiducial markers. *Image and vision Computing*, 76, 38–47.

Wolf, S., Grioli, G., Eiberger, O., Friedl, W., Grebenstein, M., Höppner, H., Burdet, E., Caldwell, D.G., Carloni, R., Catalano, M.G., and Lefeber, D. (2015). Variable stiffness actuators: Review on design and components. *IEEE/ASME Transactions on Mechatronics*, 21(5), 2418–2430.

Zhang, J., Wang, T., Wang, J., Wang, M.Y., Li, B., Zhang, J.X., and Hong, J. (2020). Geometric confined pneumatic soft-rigid hybrid actuators. *Soft Robotics*, 7(5), 574–582. doi:10.1089/soro.2019.0085.

Zhou, J., Chen, S., and Wang, Z. (2017). A soft-robotic gripper with enhanced object adaptation and grasping reliability. *IEEE Robotics and Automation Letters*, 2(4), 2287–2293.

Zhou, J., Chen, X., Li, J., Tian, Y., and Wang, Z. (2018). A soft robotic approach to robust and dexterous grasping. In *Proceedings of the 2018 IEEE International Conference on Soft Robotics*, 412–417.

Zhou, J., Chen, X., Chang, U., Lu, J.T., Leung, C.C.Y., Chen, Y., Hu, Y., and Wang, Z. (2019). A soft-robotic approach to anthropomorphic robotic hand dexterity. *IEEE Access*, 7, 101483–101495.

Zhou, J., Chen, Y., Hu, Y., Wang, Z., Li, Y., Gu, G., and Liu, Y. (2020). Adaptive variable stiffness particle phalange for robust and durable robotic grasping. *Soft Robotics*, 7(6), 743–757.

Zhou, J., Huang, J., Dou, Q., Abeel, P., and Liu, Y. (2024). A dexterous and compliant (dexco) hand based on soft hydraulic actuation for human-inspired fine in-hand manipulation. *IEEE Transactions on Robotics*.